A mechanism for mode selection in melt band instabilities

David Bercovici [a,*], John F. Rudge [b]

[a] *Yale University, Department of Geology & Geophysics, New Haven, CT, USA*
[b] *Bullard Laboratories, Department of Earth Sciences, University of Cambridge, Madingley Road, Cambridge CB3 0EZ, United Kingdom*

A B S T R A C T

The deformation of partially molten mantle in tectonic environments can lead to exotic structures, which potentially affect both melt and plate-boundary focussing. Examples of such structures are found in laboratory deformation experiments on partially molten rocks. Simple-shear and torsion experiments demonstrate the formation of concentrated melt bands at angles of around 20° to the shear plane. The melt bands form in the experiments with widths of a few to tens of microns, and a band spacing roughly an order of magnitude larger. Existing compaction theories, however, cannot predict this band width structure, let alone any mode selection, since they infer the fastest growing instability to occur for wavelengths or bands of vanishing width. Here, we propose that surface tension in the mixture, especially on a diffuse interface in the limit of sharp melt-fraction gradients, can mitigate the instability at vanishing wavelength and thus permit mode selection for finite-width bands. Indeed, the expected weak capillary forces on the diffuse interface lead to predicted mode selection at the melt-band widths observed in the experiments.

© 2015 The Authors. Published by Elsevier B.V. This is an open access article under the CC BY license (http://creativecommons.org/licenses/by/4.0/).

1. Introduction

While mantle melting only occurs within a small volume of the Earth, it plays a disproportionate role in both geochemical evolution and plate-boundary processes (see Cox et al., 1993). Indeed, the unique deformation of partial melts likely controls flow and strain focussing at both convergent and divergent plate boundaries (e.g., Spiegelman and McKenzie, 1987; Katz, 2008; Gerya and Meilick, 2011; Gerya, 2013). In particular, sheared partial melts have been demonstrated in laboratory experiments (Daines and Kohlstedt, 1997; Holtzman et al., 2003; King et al., 2010; Qi et al., 2013) to develop narrow melt bands at shallow angles (∼20°) to the direction of motion. Such melt banding may provide high-permeability pathways that strongly influence the transport of melt to the Earth's surface (Kohlstedt and Holtzman, 2009).

The observed shallow angle of these melt bands is enigmatic and has been the subject of several theoretical studies invoking two-phase compaction theory with various rheological mechanisms (Stevenson, 1989; Spiegelman, 2003; Katz et al., 2006; Takei and Holtzman, 2009; Butler, 2012; Takei and Katz, 2013; Katz and Takei, 2013; Rudge and Bercovici, 2015). An equally significant enigma is that current two-phase models cannot predict the basic melt band width, since they infer the fastest growing instability to have zero wavelength. Laboratory experiments, however, show that while the melt bands are very narrow, of order a few to tens of microns wide, and with band spacing roughly an order of magnitude wider (Holtzman et al., 2003; Holtzman and Kohlstedt, 2007; Kohlstedt and Holtzman, 2009), they are consistently not vanishingly small. The failure to predict mode selection has been a significant conundrum for understanding the physics let alone believing the theories, and is problematic for numerical simulations for which instabilities shrink to the grid-scale, and thus cannot be resolved (Katz et al., 2006; Butler, 2012; Alisic et al., 2014). Butler (2010) proposed that, in the finite strain limit, the rotation of bands through the optimal angle of growth can amplify larger wavelength bands, although as shown earlier by Spiegelman (2003) this effect depends on the initial conditions for the structure of the porosity perturbations. Takei and Hier-Majumder (2009) proposed that compaction coincident with dissolution and precipitation provides mode selection governed by a chemical diffusion length scale, which is indeed similar to the widest band spacing, although not the band widths. However, while such chemical reactions between phases are expected to be important in geological settings (Aharonov et al., 1997), their role was not evident in the laboratory experiments, which were designed to study melt channels by stress alone and avoid reaction channelization (Holtzman et al., 2003).

Here we consider two-phase compaction theory that includes capillary effects from the interface between phases, i.e., the melt

* Corresponding author.
   E-mail addresses: david.bercovici@yale.edu (D. Bercovici), jfr23@cam.ac.uk (J.F. Rudge).

and matrix (Stevenson, 1986; Bercovici et al., 2001; Bercovici and Ricard, 2003; Hier-Majumder et al., 2006), as a means for explaining mode selection. However, capillary effects at the microscopic (i.e., pore/grain) scale cannot give the necessary effect (as will be demonstrated herein). In this paper, we propose a small adjustment to existing theories that involves a diffuse interface effect, which occurs at very large gradients in melt volume fraction (e.g., Sun and Beckermann, 2004). Below we briefly develop the concept of the diffuse interface coincident with microscopic interfaces, and demonstrate how it can predict mode selection at the observed melt-band wavelengths.

2. Theory

2.1. Two-phase mixture interface and diffuse interface

Various two-phase flow theories treat the interface between phases and associated surface energy and surface tension by defining an interface area density (i.e., interface area per unit volume) α (see Ni and Beckerman, 1991; Bercovici et al., 2001). For example, if a volume δV of mixture is filled with N spherical fluid bubbles of radius r, surrounded by an opposite matrix phase, then the fluid volume fraction is $\phi = N\frac{4}{3}\pi r^3/\delta V$, while $\alpha = N4\pi r^2/\delta V$; in the same vein, the average curvature of this interface would be $d\alpha/d\phi = (d\alpha/dr)/(d\phi/dr) = 2/r$ as expected.

However if the mixture has sharp gradients in fluid fraction $\nabla\phi$, then the gradient region itself can appear as an effective or diffuse interface. Sun and Beckermann (2004) consider a diffuse interface in a mixture and invoke the formalism of phase-field theory (Anderson et al., 1998; Chen, 2002; Moelans et al., 2008) to propose an adjusted model for interface density and curvature. We appeal to some of their concepts but diverge in other respects. One important deviation is that phase-field theory only has interfaces defined by gradients in the phase variable, while we have both a background interface from a more homogeneous distribution of phases (i.e., bubbles and grains) in addition to an effective diffuse interface caused by sharp gradients in the fluid volume fraction.

Although the interface density α may be affected by a diffuse interface, only the curvature appears in the dynamics and thus we need only specify how $d\alpha/d\phi$ is altered. Indeed as shown in Appendix A, we infer an effective curvature

$$\frac{d\alpha}{d\phi} = \frac{d\mathcal{A}}{d\phi} - \frac{1}{\mathcal{A}}\nabla^2\phi \tag{1}$$

where $\mathcal{A}$ is the microscopic (pore and grain) scale interface area, which we assume is only a function of porosity (see Bercovici et al., 2001; Hier-Majumder et al., 2006). The two terms on the right of (1) are due to microscopic scale interface curvature originally described by Bercovici et al. (2001) (first term), and that due to sharp coherent structures in the porosity field (second term). For example, a coherent structure with a sharp gradient in porosity can resemble a macroscopic bubble wall separating low and high porosity regions, which then has a net effective surface tension on it. However, there is a continuum of coherent structures between weak gradients for which the diffuse interface will barely register, to sharper ones. Indeed, since $\mathcal{A}$ is a large zeroth-order term, the diffuse interface curvature term only becomes important for sharp gradients in ϕ. Equation (1) is the same as the mean curvature inferred by Sun and Beckermann (2004), however we diverge from those authors by retaining (1) as the full effective interface curvature, while they argue to remove the microscale curvature, i.e., the first term on the right of (1). We retain this term since it is responsible for driving phase self-separation and/or wetting. Indeed the 2nd term retards self-separation once the porosity gradients get very large, and leads to a steady state separation rather than run-away separation. But to allow initial capillary effects on the

pore or grain scale, we retain the micro-scale curvature term. In the end, the new effective interface curvature $d\alpha/d\phi$ can be employed in the appropriate two-phase theory (Bercovici et al., 2001; Bercovici and Ricard, 2003).

2.2. Mass conservation

Conservation of mass in two-phase continuum mechanics dictates a relation for the volume fraction ϕ_i of phase i (i.e., either phase), which, assuming both phases are incompressible and there is no mass exchange between phases, leads to

$$\frac{\partial\phi_i}{\partial t} + \nabla \cdot (\phi_i\mathbf{v}_i) = 0 \tag{2}$$

where $\mathbf{v}_i$ is the velocity of phase i. Summing these equations and noting that $\sum_i \phi_i = 1$, we arrive at

$$\nabla \cdot \bar{\mathbf{v}} = 0 \tag{3}$$

where $\bar{\mathbf{v}} = \sum_i \phi_i\mathbf{v}_i$. We can also define the unsubscripted $\phi = \phi_1$ as the volume fraction of the minor phase, here the fluid or melt phase. We also define the unsubscripted $\mathbf{v} = \mathbf{v}_2$ as the velocity of the solid or matrix phase, and $\Delta\mathbf{v} = \mathbf{v}_2 - \mathbf{v}_1$ as the phase separation velocity. We can hence recast (2) and (3) as

$$\frac{D\phi}{Dt} = (1 - \phi)\nabla \cdot \mathbf{v} \tag{4}$$

and

$$\nabla \cdot \bar{\mathbf{v}} = \nabla \cdot (\mathbf{v} - \phi\Delta\mathbf{v}) = 0 \tag{5}$$

where $D/Dt = \partial/\partial t + \mathbf{v} \cdot \nabla$ is the material derivative in the matrix frame of reference.

2.3. Dynamics

The conservation of momentum in a creeping two-phase medium is generally prescribed (following Bercovici and Ricard, 2003, 2012)

$$0 = -\phi_i\nabla\Pi_i + \nabla \cdot (\phi_i\underline{\boldsymbol{\tau}}_i) \pm c\Delta\mathbf{v}$$
$$+ \omega_i(\Delta\Pi\nabla\phi + \nabla(\gamma\alpha)) \tag{6}$$

where we neglect gravity for the application at hand, and where the internal pressure on phase i is Π_i, $\underline{\boldsymbol{\tau}}_i$ is the deviatoric stress tensor in phase i, phase density is ρ_i, c is the coefficient of drag between phases, $\Delta\Pi = \Pi_2 - \Pi_1$, γ is the surface tension on the interface between phases, α is again the interface density, and ω_i is a weighting factor (such that $\sum_i \omega_i = 1$) that accounts for how much surface tension is embedded in one phase relative to the other.

2.3.1. Constitutive laws and rheology

Since phase 1 is a melt we assume $\underline{\boldsymbol{\tau}}_1 \approx 0$ and $\omega_1 = 0$ (Bercovici and Ricard, 2003). The matrix deviatoric stress is thus denoted as $\underline{\boldsymbol{\tau}} = \underline{\boldsymbol{\tau}}_2$ and given by

$$\underline{\boldsymbol{\tau}} = 2\mu\underline{\dot{\boldsymbol{\varepsilon}}} = \mu\left(\nabla\mathbf{v} + [\nabla\mathbf{v}]^t - \frac{2}{3}\nabla \cdot \mathbf{v}\underline{I}\right) \tag{7}$$

where μ is the matrix viscosity, and $\underline{\dot{\boldsymbol{\varepsilon}}}$ is the matrix deviatoric strain-rate tensor, $[..]^t$ implies tensor transpose and $\underline{I}$ is the identity tensor. In keeping with prior analysis (Katz et al., 2006), we allow that $(1 - \phi)\mu$ is an effective viscosity given generally by

$$\mu_{\text{eff}} = (1 - \phi)\mu = \mu_0\Lambda(\phi, \dot{\varepsilon}^2)$$

$$= \mu_0 e^{-b(\phi-\phi_0)}\left(\frac{\dot{\varepsilon}^2}{\dot{\varepsilon}_0^2}\right)^{\frac{1-n}{2n}} \tag{8}$$

where n is a true or effective power-law index, b is a constant, ϕ_0 is a reference melt fraction, and $\dot{\varepsilon}^2 = \frac{1}{2}\underline{\dot{\varepsilon}} : \underline{\dot{\varepsilon}}$ is the 2nd strain-rate invariant, which has a reference or imposed value $\dot{\varepsilon}_0^2$. This rheology allows for either a dislocation creep power-law rheology where $n \approx 3$ (Katz et al., 2006), or an effective power-law rheology from grain-damage in which n can be larger than 3 (Rudge and Bercovici, 2015). Finally, significant banding instabilities appear to require a strongly nonlinear porosity-dependent viscosity, e.g., with $b \approx 25/n$ (Mei et al., 2002; Katz et al., 2006; Takei and Holtzman, 2009).

The constitutive law for the pressure difference across the interface is given by Bercovici and Ricard (2003)

$$\Delta\Pi = -\gamma \frac{d\alpha}{d\phi} - B(\phi)\frac{D\phi}{Dt} \tag{9}$$

where the 2nd term on the right accounts for viscous resistance to matrix compaction, thus B is akin to the effective bulk viscosity invoked by McKenzie (1984), and is in general a function of ϕ.

The interface drag coefficient is denoted by c and is typically proportional to the ratio of melt viscosity to matrix permeability; however, for the sake of simplicity there is no need to introduce a new variable yet, and we merely need to note that c is also a function of ϕ.

2.4. Final synthesized force balance equations

Given the assumption of inviscid melt, the force balance equation (6) for the melt (phase 1) essentially becomes Darcy's law:

$$0 = -\nabla P + c\Delta\mathbf{v}/\phi \tag{10}$$

where we define $\Pi_1 = P$ is the fluid (melt) pressure. The weighted difference of the two momentum equations (i.e., $\phi_1 = \phi$ times the equation for phase 2 minus $\phi_2 = 1 - \phi$ times the equation for phase 1) leads to

$$0 = \nabla(\mathcal{B}\nabla\cdot\mathbf{v}) + 2\mu_0\nabla\cdot(\Lambda\underline{\dot{\varepsilon}})$$
$$- c\Delta\mathbf{v}/\phi + \gamma\nabla\left(\alpha + (1-\phi)\frac{d\alpha}{d\phi}\right) \tag{11}$$

where we define $\mathcal{B} = (1-\phi)^2 B(\phi)$. Using the arguments outlined in Section 2.1, the last term on the right of (11) is

$$\gamma\nabla\left(\alpha + (1-\phi)\frac{d\alpha}{d\phi}\right)$$
$$= \gamma(1-\phi)\left(\frac{d^2\mathcal{A}}{d\phi^2}\nabla\phi - \frac{1}{\mathcal{A}}\nabla(\nabla^2\phi) + \frac{1}{\mathcal{A}^2}\frac{d\mathcal{A}}{d\phi}(\nabla^2\phi)\nabla\phi\right) \tag{12}$$

The first term on the right side of (12) provides an effective pressure gradient due to variations in microscopic interface curvature, which can, depending on the sign of $d^2\mathcal{A}/d\phi^2$, either lead to self-separation of phases (if the sign is negative; see Ricard et al., 2001; Bercovici and Ricard, 2003) or dispersal of phases via wetting of grain-boundaries (if the sign is positive; see Hier-Majumder et al., 2006) as generally happens in low-melt fraction partial melts (e.g., Parsons et al., 2008; King et al., 2011, and references therein). The second two terms on the right of (12) together represent a pressure gradient caused by variations in the surface tension on effective macroscopic (diffuse) interfaces associated with sharp gradients in ϕ. In particular, high pressure zones are caused by the surface tension around porosity anomalies with large functional curvature $\nabla^2\phi$ (which thus act, for example, like effective bubbles of high porosity), and the resulting pressure gradient acts to smooth out the porosity anomalies and mitigate the development of sharp porosity features. However the nonlinear contributions to this effect, in particular the third term on the right of (12), do not influence the linear stability analysis presented herein.

3. Linear analysis of simple shear experiments

As a representation of the shear-band experiments (Holtzman et al., 2003; Kohlstedt and Holtzman, 2009), we assume the model system is in simple shear in the x direction with steady velocity given by

$$\mathbf{v}_0 = u(y)\hat{\mathbf{x}} = 2y\dot{\varepsilon}_0\hat{\mathbf{x}} \tag{13}$$

where $\dot{\varepsilon}_0$ is an imposed shear strain-rate. The basic steady state is assumed uniform and constant, with no phase separation (i.e., both phases move at velocity $\mathbf{v}_0$). We consider two-dimensional (2-D) infinitesimal perturbations to the basic state in the horizontal x–y plane, in which case, the dependent variables become

$$\phi = \phi_0 + \epsilon\varphi_1 \tag{14a}$$

$$\mathbf{v} = \mathbf{v}_0(y) + \epsilon(\nabla\vartheta_1 + \nabla\times(\psi_1\hat{\mathbf{z}})) \tag{14b}$$

$$\Delta\mathbf{v} = \epsilon\Delta\mathbf{v}_1 \tag{14c}$$

$$\Lambda = \Lambda_0 + \epsilon\Lambda_1 = 1 - \epsilon\left(b\varphi_1 + q\frac{\dot{\varepsilon}_{1xy}}{\dot{\varepsilon}_0}\right) \tag{14d}$$

where $\epsilon \ll 1$, ϑ_1 is a flow potential, ψ_1 is a stream function, and $q = 1 - 1/n$. All zeroth order variables are uniform and constant except for $\mathbf{v}_0$ which is a function of y, and all first order variables are functions of x, y and time t. We first substitute (14) into (4), and into both $\nabla\cdot$ and $\hat{\mathbf{z}}\cdot\nabla\times$ of (11), using (5) and (10) to eliminate $\Delta\mathbf{v}$. This yields governing equations for the perturbations of $O(\epsilon^1)$, which we then non-dimensionalize by scaling time by $(2\dot{\varepsilon}_0)^{-1}$, and distance by the compaction length

$$\delta = \sqrt{\phi_0^2(\mathcal{B}_0 + \tfrac{4}{3}\mu_0)/c_0} \tag{15}$$

where $\mathcal{B}_0 = \mathcal{B}(\phi_0)$ and $c_0 = c(\phi_0)$. The dimensionless governing perturbation equations become, after some algebra

$$\frac{D_0\varphi_1}{Dt} = (1-\phi_0)\nabla^2\vartheta_1 \tag{16a}$$

$$(\nabla^4 - \nabla^2)\vartheta_1 = \nu\left(\Gamma(\mathcal{D}\nabla^4 - \nabla^2)\varphi_1 - 2\frac{\partial^2\Lambda_1}{\partial x\partial y}\right) \tag{16b}$$

$$\nabla^4\psi_1 = \triangle^*\Lambda_1 \tag{16c}$$

$$\Lambda_1 = -b\varphi_1 + q\left(\triangle^*\psi_1 - 2\frac{\partial^2\vartheta_1}{\partial x\partial y}\right) \tag{16d}$$

where $\triangle^* = \frac{\partial^2}{\partial x^2} - \frac{\partial^2}{\partial y^2}$, and

$$\nu = \frac{\mu_0}{\mathcal{B}_0 + \frac{4}{3}\mu_0} \tag{17a}$$

$$\Gamma = \frac{\gamma(1-\phi_0)\mathcal{A}_0''}{2\dot{\varepsilon}_0\mu_0} \tag{17b}$$

$$\mathcal{D} = (\mathcal{A}_0''\mathcal{A}_0\delta^2)^{-1} \tag{17c}$$

in which $\mathcal{A}_0 = \mathcal{A}(\phi_0)$ and $\mathcal{A}_0'' = [d^2\mathcal{A}/d\phi^2]_{\phi_0}$.

3.1. Normal mode analysis and dispersion relation

In the usual method of normal mode analysis, we assume all dependent variables go as $e^{-i\mathbf{k}\cdot\mathbf{x}+st}$ where $\mathbf{k} = (k_x, k_y) = k(\cos\theta, \sin\theta)$ is the wave vector in which θ is the wave-vector angle, $\mathbf{x} = (x, y)$ is the position vector, and s is the growth rate. Substituting this relation into (16), and solving for s leads to the dispersion relation
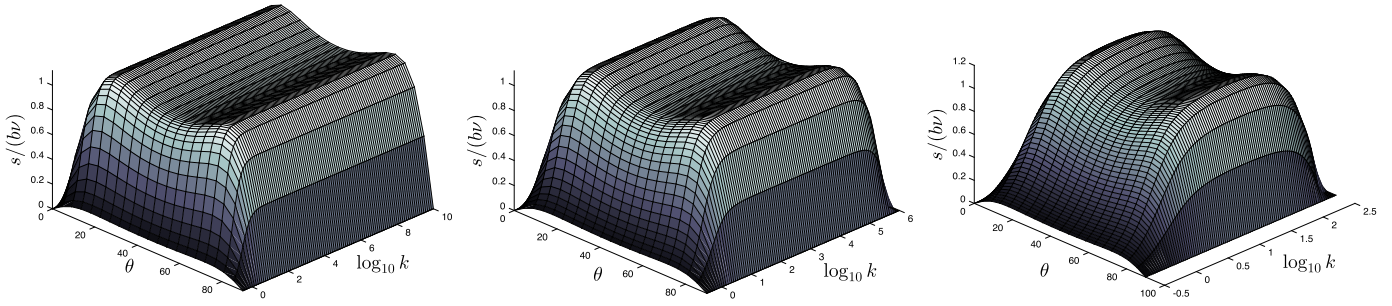
Fig. 1. Growth s vs wave-number k and wave-vector angle θ from (18). The left and middle panels are for $\mathcal{D} = 0$ and $\mathcal{D} = 10^{-8}$, respectively, and both have $\mathcal{Q} = b/\Gamma = 10^4$ (the left panel is also arbitrarily truncated at $k = 10^{10}$); the right panel is for $\mathcal{Q} = 10^3$ and $\mathcal{D} = 10^{-2}$. The case for $\mathcal{D} = 0$ (left panel) does not have peak growth at a finite k and thus does not allow mode selection, unlike the cases for $\mathcal{D} > 0$. All three cases have the same values of $\phi_0 = 0.05$, $n = 4$, $\nu = 3\phi_0/4$.

$$s = (1 - \phi_0)\nu\Gamma k^2$$
$$\cdot \frac{\mathcal{Q}\sin(2\theta) - (1 + \mathcal{D}k^2)(1 - q\cos^2(2\theta))}{(1 + k^2)(1 - q\cos^2(2\theta)) - q\nu k^2 \sin^2(2\theta)} \quad (18)$$

where we define $\mathcal{Q} = b/\Gamma$ (see Fig. 1). Here we have neglected the advection term in (16a); inclusion of advection does not change the basic results but simply breaks the degeneracy of mode selection in θ in favor of shallow-angled bands (Spiegelman, 2003; Katz et al., 2006; Rudge and Bercovici, 2015).

The influence of shear deformation is represented in the numerator of (18) by the term that goes as $\Gamma\mathcal{Q} = b$, modulated by non-Newtonian effects in the denominator, but which is then always positive. The effect of surface tension is contained in the factor that goes as $\Gamma + \Gamma\mathcal{D}k^2$, whose two terms represent microscopic and diffuse-interface capillary effects, respectively. Only the microscopic capillary term depends on microscopic interface curvature $\mathcal{A}_0''$, which can either be negative for self-separation (Ricard et al., 2001) (that would then accelerate the banding instability), or positive for wetting and melt dispersal (Hier-Majumder et al., 2006) (that then, like the diffuse-interface effect, retards the instability). Here we assume $\mathcal{A}_0'' >$ for the wetting case, which is typical of partial melts (Parsons et al., 2008; King et al., 2011). However, only the diffuse interface effect permits mode selection. For example, in the limits of $k^2 \to 0$ and $k^2 \to \infty$, $s \to 0$ and $s \to -\infty$, respectively, but has positive values in between these limits, and thus a least-stable mode exists at some finite k. If there is no diffuse interface effect such that $\mathcal{D} = 0$, then s goes to a positive asymptote as $k^2 \to \infty$ and there is no selected mode (Fig. 1). Thus only the introduction of diffuse interface surface tension allows for mode selection at finite wavelength; microscopic capillary forces (even if causing wetting and melt dispersal) by themselves will not allow for mode selection. Although the mode selection is very broad for expected parameter values, in which $\mathcal{Q} \gg 1$ and $\mathcal{D} \ll 1$ (Fig. 1) these same parameters lead to a very high wavenumber k, or small wavelength, selection, as discussed next.

3.1.1. Least stable mode

We can gain some immediate intuition about mode selection if we first consider the simplest case of a Newtonian matrix rheology, whence $q = 0$, in which case the growth rate is necessarily maximum at $\theta = \pi/4$ (i.e., bands at $45°$ angles), and thus

$$s = (1 - \phi_0)\nu\Gamma k^2 \cdot \frac{\mathcal{Q} - (1 + \mathcal{D}k^2)}{1 + k^2} \quad (19)$$

Marginal stability occurs for $s = 0$, which implies a critical value of $\mathcal{Q} = 1 + \mathcal{D}k^2$ above which perturbations are unstable. The least stable mode, for which $ds/dk^2 = 0$, occurs at a wave-number given by

$$k_m^2 = \sqrt{1 + (\mathcal{Q} - 1)/\mathcal{D}} - 1 \quad (20)$$

However, as discussed in Section 4.1, typical experimental conditions and properties lead to $\mathcal{Q} \gg 1$ and $\mathcal{D} \ll 1$ and thus $k_m \approx (\mathcal{Q}/\mathcal{D})^{1/4}$, which, while not infinite, is intrinsically a large number and thus leads to small wavelengths. At this wavenumber, the approximate growth rate from (19) (noting that typically $\mathcal{Q}\mathcal{D} \ll 1$ such that $\mathcal{D}k_m^2 \ll 1$) is $s_m \approx (1 - \phi_0)b\nu$, which is typically $O(1)$ (again see Section 4.1), and thus the dimensional growth rate is roughly equal to the imposed strain-rate. These simple scaling results for the least stable mode and associated growth rate hold for the general case except for an angular dependence as well as influence of $q \neq 0$, for which the least stable mode does not occur at $\theta = \pi/4$.

For the general case of $q \neq 0$ and arbitrary fixed θ, the least stable mode is given by

$$k_m^2 = \frac{\sqrt{1 + \frac{1}{\mathcal{D}}(\frac{\mathcal{Q}S}{C^2} - 1)(1 - \frac{q\nu S^2}{C^2})} - 1}{1 - \frac{q\nu S^2}{C^2}} \quad (21)$$

where we have defined

$$S = \sin(2\theta) \quad \text{and} \quad C^2 = 1 - q\cos^2(2\theta) \quad (22)$$

(see Fig. 2). Again, taking the asymptotic limits $\mathcal{Q} \gg 1$ and $\mathcal{D} \ll 1$, and in addition $q\nu S^2/C^2 \ll 1$ (since $\nu \sim \phi_0 \ll 1$; see Section 4.1), the least-stable wave-number and associated growth rate are

$$k_m \approx \left(\frac{\mathcal{Q}S}{\mathcal{D}C^2}\right)^{1/4} \quad \text{and} \quad s_m \approx (1 - \phi_0)\frac{b\nu S}{C^2} \quad (23)$$

(see Fig. 2).

The dependences on θ and $q = 1 - 1/n$ for both k_m and s_m are contained in the ratio S/C^2. Thus the angle θ at which maximum growth occurs is given by $d(SC^{-2})/d\theta = 0$ which leads to $\theta_m = \frac{1}{2}\sin^{-1}(\pm\sqrt{1/(n-1)})$, which is effectively the same result as found by Katz et al. (2006). At this value of θ_m, $S/C^2 = n/(2\sqrt{n-1})$, which is typically $O(1)$. For example, using $n = 4$, $\theta_m \approx 18°$ and $72°$ (e.g., see Fig. 2) and $S/C^2 = 2/\sqrt{3} \approx 1$. (Note, however, for $n \leq 2$ the only real angle allowed is $\theta_m = 45°$; see Katz et al., 2006.) In general the angular and rheological power-law dependence of the least-stable mode does not change with the introduction of the diffuse interface effect, which itself simply allows for a finite wavelength $2\pi/k_m$ to be selected. Thus for the least stable angle θ, the least stable mode is still given by $k_m \approx (\mathcal{Q}/\mathcal{D})^{1/4} \gg 1$, and the associated growth rate is $s_m \approx (1 - \phi_0)b\nu \approx O(1/n)$ (since $b \approx 25/n$).
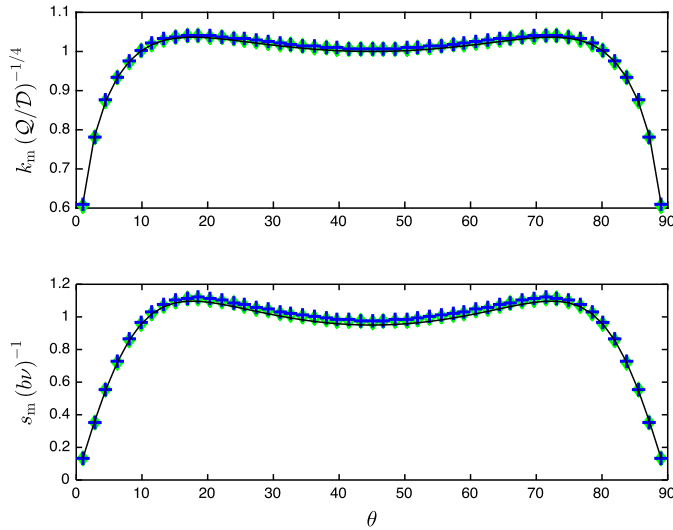
Fig. 2. Least stable wavenumber k_m from (21) (top) and associated growth rate s_m from (18) (bottom) versus wave-vector angle θ, for the same cases as in Fig. 1 for $\mathcal{D} \neq 0$, shown as green and blue symbols. The thin black curves are the asymptotic relations given in (23); given the proper scaling these relations are sufficient to describe the least stable modes. (For interpretation of the references to color in this figure legend, the reader is referred to the web version of this article.)

4. Discussion and conclusion: application to melt band experiments

4.1. Scales and numbers for mode selection

The dimensionless numbers for the governing equations depend on various experimental parameters. We consider two cases in the shear-banding experiments of Holtzman et al. (2003, see Table 1) (see also Kohlstedt and Holtzman, 2009): (1) an anorthosite matrix with a low-viscosity MORB (mid-ocean ridge basalt) melt, and (2) an olivine matrix with a high viscosity albite melt, both of which led to shallow shear bands with 15–20° angles, but with significantly different band widths and spacing. For the anorthosite + MORB case, the imposed strain-rate was $\dot{\varepsilon}_0 = 3 \times 10^{-4}$ s^{-1}, the matrix viscosity (which we assume to be the same as the basic-state viscosity) was $\mu_0 = 6 \times 10^{11}$ Pa s, the melt viscosity was $\mu_f = 10$ Pa s, the mean melt volume fraction was $\phi_0 = 0.03$, the matrix permeability was $\mathsf{k} = 10^{-17}$ m^2 and the grain-size radius was $r = 2$ μm. In the olivine + albite-melt case, $\dot{\varepsilon}_0 = 3 \times 10^{-3}$ s^{-1}, $\mu_0 = 5 \times 10^{12}$ Pa s, $\mu_f = 3.3 \times 10^5$ Pa s, $\phi_0 = 0.03$, $\mathsf{k} = 4 \times 10^{-17}$ m^2, and $r = 4$ μm.

To evaluate our model dimensionless parameters, we use $\mathcal{B}_0 = (1 - \phi_0)^2 B_0 = \frac{4}{3} \mu_0 (1 - \phi_0)/\phi_0$ (see Bercovici et al., 2001; Bercovici and Ricard, 2003); thus $\mathcal{B}_0 + \frac{4}{3} \mu_0 = \frac{4}{3} \mu_0/\phi_0$ in which case (17) leads to $\nu = \frac{3}{4} \phi_0$. (Note that our estimates of ν and compaction length δ differ from that used by Holtzman et al. (2003) who effectively assumed $\mathcal{B}_0 \ll \mu_0$.)

For the parameters $\mathcal{Q} = b/\Gamma$ and $\mathcal{D}$, we use a typical surface tension $\gamma \approx 1$ Pa m, $b = 25/n$ (Mei et al., 2002; Takei and Holtzman, 2009), and $c_0 = \mu_f \phi_0^2/\mathsf{k}$. We can approximate the microscopic interface area density $\mathcal{A}_0$ for a mixture of simple spherical or regular-polyhedral grains of mean size r embedded in a small amount of melt, in which case $\mathcal{A}_0 \approx 3/r$ (Bercovici et al., 2001; Bercovici and Ricard, 2012; Ricard and Bercovici, 2009). As noted already, the microscopic curvature $\mathcal{A}_0''$ can be positive or negative depending on whether the mixture self-separates (Ricard et al., 2001) or undergoes grain-boundary wetting (Hier-Majumder et al., 2006), although its sign has no impact on this analysis, since neither the maximum growth rate s_m nor least stable mode k_m, as given in (23), depend on $\mathcal{A}_0''$. However, the magnitude of $\mathcal{A}_0''$ is

important for estimating the dimensionless numbers $\mathcal{Q}$ and $\mathcal{D}$; in this case we approximate this quantity for that of a spherical grain, in which case $\mathcal{A}_0'' = 2/r$. Thus using (17),

$$\mathcal{Q} = \frac{b}{\Gamma} = \frac{b \mu_0 \dot{\varepsilon}_0 r}{\gamma (1 - \phi_0)} \approx 10^4 \text{ and } 10^6 \tag{24a}$$

$$\mathcal{D} = \frac{\mu_f \phi_0 r^2}{8 \mu_0 \mathsf{k}} \approx 3 \times 10^{-8} \text{ and } 10^{-4} \tag{24b}$$

where the two values of each parameter are for the anorthosite + MORB and olivine + albite-melt experiments, respectively. In estimating $\mathcal{Q}$, we have assumed diffusion creep, hence $n = 1$, for lack of any information to the contrary in the experiments. Values of $n > 1$ allow for shallow angled melt bands (i.e., $\theta < 45°$), but only influence mode selection through the relation $b = 25/n$, which would reduce $\mathcal{Q}$ and the growth rate s_m by a factor of n, and the least stable wavenumber k_m by $n^{1/4}$.

4.2. Mode selection and comparison to experiments

With the dimensionless numbers inferred above, we indeed see that $\mathcal{Q} \gg 1$ and $\mathcal{D} \ll 1$; thus the least stable mode and associated growth rate are given by (23). The dimensionless growth rate for both experimental cases of anorthosite + MORB and olivine + albite-melt is the same (since b and ϕ_0 are the same for each) and yields $s_\mathrm{m} \approx 0.5$. For the anorthosite + MORB case, the dimensionless least-stable mode wavenumber is $k_\mathrm{m} \approx 800$; thus, given a compaction length $\delta \approx 5000$ μm, the dimensional least-stable mode wavelength is $\lambda_m = 2\pi \delta/k_m \approx 40$ μm. For the olivine + albite-melt case, $k_\mathrm{m} \approx 350$ and $\delta \approx 200$ μm, thus $\lambda_m \approx 4$ μm.

The melt bands for the anorthosite + MORB experiments were of order 20 μm wide, but separated by about 100 μm; for the olivine + albite-melt experiments, the melt bands were a few grains or microns wide, and spaced by about 20 μm (Holtzman et al., 2003; Kohlstedt and Holtzman, 2009). The melt-band widths compare favorably with the model predictions for which the band-widths would be $\lambda_m/2$; however, the band spacing is considerably wider than λ_m.

The difference between the melt band widths and their spacing in each case indicates two dominant length scales of the instability; this cannot be explained by our linear stability theory, which only predicts one least-stable mode. That the spacing is wider than the band width possibly reflects a nonlinear effect whereby the melt-rich bands drain melt from the surrounding matrix, but only as far away as some larger fraction of the compaction length; however, this assumption needs testing with nonlinear models with our proposed mechanism. Alternatively, the wide spacing could reflect the chemical-diffusion limited instability proposed by Takei and Hier-Majumder (2009) or the effect of finite strain and rotation (e.g., Butler, 2010).

The dependence of melt-band width on shear stress indicated in the experiments of Holtzman and Kohlstedt (2007) also corresponds at least qualitatively to our model predictions. The relation for the least-stable mode, e.g., (23), implies that band width goes as (stress)$^{-1/4}$, which is roughly borne out for the "constant rate" (CR) cases – which are most appropriate for our model – discussed by Holtzman and Kohlstedt (2007), although the data is sparse. Holtzman and Kohlstedt (2007), Kohlstedt and Holtzman (2009) also documented the relation between melt-band spacing and compaction length, which is qualitatively in line with our model predictions assuming band spacing and width are proportional.

In the end, the very small experimental melt-band length scales are predicted by our model to be due to a weak diffuse-interface capillary effect (represented by the dimensionless number $\mathcal{D}$),
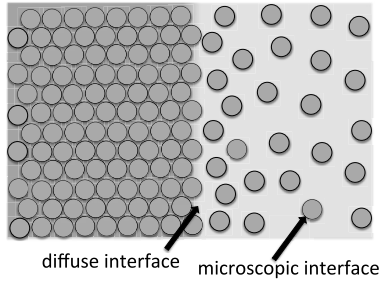
Fig. 3. Simple sketch of an abrupt transition in porosity from packed to dispersed spherical grains (grey circles) in partial melt, to illustrate both microscopic and diffuse interfaces.

which does not damp growth of the shear-band instability until very large wave numbers or small wavelengths. Our predictions closely match the narrow experimental melt-band widths, but more work is needed to understand the wider spacing between melt bands.

Acknowledgements

Appendix A. Distribution function and effective curvature near a diffuse interface

In a two-phase mixture, the volume fraction of each phase and the interface between them is fundamentally described by a distribution, or existence, function Θ which is effectively a spacial box-car function that is unity in one phase and zero in the other. In our two-phase model, if $\Theta = 1$ for phase 1, then volume fractions and interface density are (e.g., Ni and Beckerman, 1991; Bercovici et al., 2001)

$$\phi_1 = \frac{1}{\delta V} \int_{\delta V} \Theta \, dV, \qquad \phi_2 = \frac{1}{\delta V} \int_{\delta V} (1 - \Theta) \, dV \quad \text{and}$$

$$\mathcal{A} = \frac{1}{\delta V} \int_{\delta V} |\nabla \Theta| \, dV \qquad (A.1)$$

where δV is pseudo-infinitesimal volume (i.e., small enough to resolve spatial gradients but big enough to enclose a statistically meaningful sample of drops, pores and/or grains of the two phases). Typically Θ is assumed to be comprised of fine scale 3-D boxcars whose distribution varies smoothly over δV. Moreover, the effective mean curvature of the fine scale interface is $d\mathcal{A}/d\phi$ (e.g., Ni and Beckerman, 1991; Bercovici et al., 2001).

However in the melt-band experiments, the final band instabilities are several tens of melt pores and grains wide and that structure is small enough to affect the shape of Θ at an intermediate scale (i.e., between the pore/grain scale and the larger spatial scales resolved by δV). In particular we consider that at this intermediate scale, Θ is influenced by sharp gradients in ϕ, i.e., where the length scale of the gradients becomes comparable to that of the control volume δV and not much bigger than the bubble or grain sizes. Thus, we consider Θ in the vicinity of a mean structure or coherent diffuse-interface imposed by a sharp gradient in ϕ and seek the effective interface curvature near this structure (see Fig. 3).

Curvature of an interface with unit normal $\hat{\mathbf{n}}$ is simply $\nabla \cdot \hat{\mathbf{n}}$; here we define $\hat{\mathbf{n}}$ to point away from the fluid (where $\Theta = 1$) into

the solid matrix (where $\Theta = 0$) and thus $\hat{\mathbf{n}} = -\nabla \Theta / |\nabla \Theta|$ such that the curvature is

$$\kappa = \nabla \cdot \hat{\mathbf{n}} = -\frac{1}{|\nabla \Theta|} \left(\nabla^2 \Theta - \frac{\partial^2 \Theta}{\partial n^2} \right)$$

$$\text{where } \frac{\partial^2 \Theta}{\partial n^2} = \hat{\mathbf{n}} \cdot \nabla (\hat{\mathbf{n}} \cdot \nabla \Theta) \qquad (A.2)$$

Following Sun and Beckermann (2004), we next define the mean curvature along the interface as $\bar{\kappa} = \langle \kappa |\nabla \Theta| \rangle / \langle |\nabla \Theta| \rangle$ where $\langle q \rangle$ is the volume average of any quantity q over a control volume δV, as described in (A.1). The mean curvature is thus

$$\bar{\kappa} = -\frac{1}{\langle |\nabla \Theta| \rangle} \left\langle \nabla^2 \Theta - \frac{\partial^2 \Theta}{\partial n^2} \right\rangle$$

$$= -\frac{1}{\mathcal{A}} \left(\langle \nabla^2 \Theta \rangle - \left\langle \frac{\partial^2 \Theta}{\partial n^2} \right\rangle \right) \qquad (A.3)$$

where we have used (A.1) to introduce the factor of $1/\mathcal{A}$. We now consider the two terms on the far right of (A.3) separately for both a uniform (within a control volume) medium of dispersed (i.e., non-contacting) identical spherical fluid bubbles, and then also for the influence of the coherent structure with a sharp porosity gradient. For one bubble of radius a, $\Theta = 1$ for $r < a$, and $\Theta = 0$ for $r > a$, where r is the radial position from the bubble's center. In this case

$$\nabla \Theta = -\delta(r - a)\hat{\mathbf{r}}, \qquad \nabla^2 \Theta = -\frac{2}{r}\delta(r - a) - \delta'(r - a), \quad \text{and}$$

$$\frac{\partial^2 \Theta}{\partial n^2} = \frac{\partial^2 \Theta}{\partial r^2} = -\delta'(r - a) \qquad (A.4)$$

If we have N such bubbles dispersed in the control volume, it can be readily shown that $\langle |\nabla \Theta| \rangle = \mathcal{A} = N 4\pi a^2 / \delta V$ as expected, and $\langle \nabla^2 \Theta \rangle = 0$ while $\langle \partial^2 \Theta / \partial n^2 \rangle = N 8\pi a / \delta V$. In total, the microscopic contribution to the mean curvature $\bar{\kappa}$ is simply $2/a$, but only the second term on the far right of (A.3) contributes to the mean microscopic curvature.

In the vicinity of a coherent structure with a sharp gradient in ϕ, $\langle \nabla^2 \Theta \rangle = \nabla^2 \phi$ (provided that $\nabla \Theta$ averaged over any surface element of the control volume δV varies no more than linearly perpendicular to that element; see Bercovici et al., 2001). Moreover, the control volume can be chosen small enough to render the coherent structure a flat diffuse surface or boundary layer inside that volume; since $\partial^2 \Theta / \partial n^2$ is an odd function centered on that structure, then $\langle \partial^2 \Theta / \partial n^2 \rangle = 0$.

Summing the effects of the microscopic and coherent structures together, we see that only the coherent structure contributes to the first term on the far right side of (A.3), while only the microscopic structure contributes to the second term. Therefore, the final average curvature (A.3) associated with both the microscopic background value and that due to the coherent structure is

$$\frac{d\alpha}{d\phi} = \bar{\kappa} = \frac{d\mathcal{A}}{d\phi} - \frac{1}{\mathcal{A}} \nabla^2 \phi \qquad (A.5)$$

where we have associated $d\mathcal{A}/d\phi$ with the mean microscopic curvature $2/a$, and we note that (A.5) is the same as that derived by Sun and Beckermann (2004). In the end, we infer that with both finer and coarse scale structures in the distribution function Θ, the effective interface curvature is given by (A.5), which is the starting point for our model with equation (1).

References

Aharonov, E., Spiegelman, M., Kelemen, P., 1997. Three-dimensional flow and reaction in porous media: implications for the Earth's mantle and sedimentary basins. J. Geophys. Res. 102, 14821–14834.

Alisic, L., Rudge, J.F., Katz, R.F., Wells, G.N., Rhebergen, S., 2014. Compaction around a rigid, circular inclusion in partially molten rock. J. Geophys. Res., Solid Earth 119 (7), 5903–5920. http://dx.doi.org/10.1002/2013JB010906.

Anderson, D.M., McFadden, G.B., Wheeler, A.A., 1998. Diffuse-interface methods in fluid mechanics. Annu. Rev. Fluid Mech. 30 (1), 139–165. http://dx.doi.org/10.1146/annurev.fluid.30.1.139.

Bercovici, D., Ricard, Y., 2003. Energetics of a two-phase model of lithospheric damage, shear localization and plate-boundary formation. Geophys. J. Int. 152, 581–596.

Bercovici, D., Ricard, Y., 2012. Mechanisms for the generation of plate tectonics by two-phase grain-damage and pinning. Phys. Earth Planet. Inter. 202–203, 27–55.

Bercovici, D., Ricard, Y., Schubert, G., 2001. A two-phase model of compaction and damage, 1. General theory. J. Geophys. Res. 106 (B5), 8887–8906.

Butler, S., 2010. Porosity localizing instability in a compacting porous layer in a pure shear flow and the evolution of porosity band wavelength. Phys. Earth Planet. Inter. 182 (1–2), 30–41. http://www.sciencedirect.com/science/article/pii/S003192011000124X.

Butler, S.L., 2012. Numerical models of shear-induced melt band formation with anisotropic matrix viscosity. Phys. Earth Planet. Inter. 200–201, 28–36.

Chen, L.-Q., 2002. Phase-field models for microstructure evolution. Annu. Rev. Mater. Sci. 32 (1), 113–140. http://dx.doi.org/10.1146/annurev.matsci.32.112001.132041.

Cox, K., McKenzie, D., White, R., 1993. Melting and Melt Movement in the Earth. Oxford University Press, New York, NY. First published in Philos. Trans. R. Soc., Ser. A 342, 1–91.

Daines, M.J., Kohlstedt, D.L., 1997. Influence of deformation on melt topology in peridotites. J. Geophys. Res. 102, 10257–10271.

Gerya, T.V., 2013. Three-dimensional thermomechanical modeling of oceanic spreading initiation and evolution. Phys. Earth Planet. Inter. 214, 35–52. http://www.sciencedirect.com/science/article/pii/S0031920112001835.

Gerya, T.V., Meilick, F.I., 2011. Geodynamic regimes of subduction under an active margin: effects of rheological weakening by fluids and melts. J. Metamorph. Geol. 29 (1), 7–31. http://dx.doi.org/10.1111/j.1525-1314.2010.00904.x.

Hier-Majumder, S., Ricard, Y., Bercovici, D., 2006. Role of grain boundaries in magma migration and storage. Earth Planet. Sci. Lett. 248, 735–749.

Holtzman, B.K., Groebner, N.J., Zimmerman, M.E., Ginsberg, S.B., Kohlstedt, D.L., 2003. Stress-driven melt segregation in partially molten rocks. Geochem. Geophys. Geosyst. 4 (5). http://dx.doi.org/10.1029/2001GC000258.

Holtzman, B.K., Kohlstedt, D.L., 2007. Stress-driven melt segregation and strain partitioning in partially molten rocks: effects of stress and strain. J. Petrol. 48 (12), 2379–2406. http://petrology.oxfordjournals.org/content/48/12/2379.abstract.

Katz, R.F., 2008. Magma dynamics with the enthalpy method: benchmark solutions and magmatic focusing at mid-ocean ridges. J. Petrol. 49 (12), 2099–2121.

Katz, R.F., Spiegelman, M., Holtzman, B., 2006. The dynamics of melt and shear localization in partially molten aggregates. Nature 442 (7103), 676–679. http://dx.doi.org/10.1038/nature05039.

Katz, R.F., Takei, Y., 2013. Consequences of viscous anisotropy in a deforming, two-phase aggregate. Part 2. Numerical solutions of the full equations. J. Fluid Mech. 734, 456–485.

King, D.S., Hier-Majumder, S., Kohlstedt, D.L., 2011. An experimental study of the effects of surface tension in homogenizing perturbations in melt frac-

tion. Earth Planet. Sci. Lett. 307 (3–4), 349–360. http://www.sciencedirect.com/science/article/pii/S0012821X11002809.

King, D.S.H., Zimmerman, M.E., Kohlstedt, D.L., 2010. Stress-driven melt segregation in partially molten olivine-rich rocks deformed in torsion. J. Petrol. 51, 21–42.

Kohlstedt, D.L., Holtzman, B.K., 2009. Shearing melt out of the Earth: an experimentalist's perspective on the influence of deformation on melt extraction. Annu. Rev. Earth Planet. Sci. 37, 561–593.

McKenzie, D., 1984. The generation and compaction of partially molten rock. J. Petrol. 25, 713–765.

Mei, S., Bai, W., Hiraga, T., Kohlstedt, D., 2002. Influence of melt on the creep behavior of olivine–basalt aggregates under hydrous conditions. Earth Planet. Sci. Lett. 201 (3–4), 491–507. http://dx.doi.org/10.1016/S0012-821X(02)00745-8.

Moelans, N., Blanpain, B., Wollants, P., 2008. An introduction to phase-field modeling of microstructure evolution. Calphad 32 (2), 268–294. http://dx.doi.org/10.1016/j.calphad.2007.11.003.

Ni, J., Beckerman, C., 1991. A volume-averaged two-phase model for transport phenomena during solidification. Metall. Trans. B 22, 349–361.

Parsons, R., Nimmo, F., Hustoft, J., Holtzman, B., Kohlstedt, D., 2008. An experimental and numerical study of surface tension-driven melt flow. Earth Planet. Sci. Lett. 267 (3–4), 548–557. http://www.sciencedirect.com/science/article/pii/S0012821X07008023.

Qi, C., Zhao, Y.-H., Kohlstedt, D.L., 2013. An experimental study of pressure shadows in partially molten rocks. Earth Planet. Sci. Lett. 382, 77–84.

Ricard, Y., Bercovici, D., 2009. A continuum theory of grain size evolution and damage. J. Geophys. Res. 114, B01204. http://dx.doi.org/10.1029/2007JB005491.

Ricard, Y., Bercovici, D., Schubert, G., 2001. A two-phase model of compaction and damage, 2, applications to compaction, deformation, and the role of interfacial surface tension. J. Geophys. Res. 106 (B5), 8907–8924.

Rudge, J.F., Bercovici, D., 2015. Melt-band instabilities with two-phase grain-damage. Geophys. J. Int. 201, 640–651.

Spiegelman, M., 2003. Linear analysis of melt band formation by simple shear. Geochem. Geophys. Geosyst. 4, 8615.

Spiegelman, M., McKenzie, D., 1987. Simple 2-d models for melt extraction at mid-ocean ridges and island arcs. Earth Planet. Sci. Lett. 83, 137–152.

Stevenson, D., 1986. On the role of surface tension in the migration of melts and fluids. Geophys. Res. Lett. 13, 1149–1152.

Stevenson, D.J., 1989. Spontaneous small-scale melt segregation in partial melts undergoing deformation. Geophys. Res. Lett. 16, 1067–1070.

Sun, Y., Beckermann, C., 2004. Diffuse interface modeling of two-phase flows based on averaging: mass and momentum equations. Physica D 198, 281–308.

Takei, Y., Hier-Majumder, S., 2009. A generalized formulation of interfacial tension driven fluid migration with dissolution/precipitation. Earth Planet. Sci. Lett. 288 (1–2), 138–148. http://dx.doi.org/10.1016/j.epsl.2009.09.016.

Takei, Y., Holtzman, B., 2009. Viscous constitutive relations of solid–liquid composites in terms of grain boundary contiguity: 3. Causes and consequences of viscous anisotropy. J. Geophys. Res. 114, B06207.

Takei, Y., Katz, R.F., 2013. Consequences of viscous anisotropy in a deforming, two-phase aggregate. Part 1. Governing equations and linearized analysis. J. Fluid Mech. 734, 424–455.